Workshop on Cartan Geometries, March 4 – 8, 2024

Université d'Orsay

The primary visual cortex as a Cartan engine

Jean Petitot,
CAMS, EHESS, Paris,
jean.petitot@ehess.fr

1. Introduction

This talk is not about new results on geometry "à la Cartan", but about the way in which this type of geometry comes into play when we want to explain how the brain can do geometry.

It will have two parts.
A part on experimental neural results.
A part with pictures of the sub-Riemannian geometry of $SE(2)$ the group of direct isometries of the plane (the retinal plane in our models)

2. Introduction

Our visual perception is an excellent geometer and since ancient times intuitive perceptual geometry has served as the basis for many aspects of mathematical geometry.

Since Gestalt theory, an enormous amount of phenomenological, psychological and psychophysical data has been accumulated on these extraordinary abilities, which have arisen from biological evolution since the appearance in primitive organisms of the first cells containing photosensitive opsins.

3. Introduction

We know that the structures of perceptual geometry are implemented neurally and we know more or less *where* thanks to numerous experimental data on the effects of localised lesions.

We know that basic perceptions such as lines, crossings, corners, curvatures, surfaces contoured by these edges, etc. are implemented in areas of the occipital primary visual cortex.

The retinal signal is pixelised. There is no global geometric structuring prior to cortical processes.

4. The visual brain

Here is an image of the human brain. It shows the neural pathways from the retina to the lateral geniculate nucleus (LGN thalamic relay) and then to the occipital primary visual cortex (area $V1$).

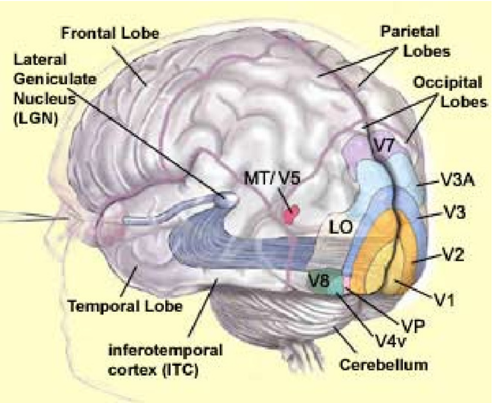

5. Introduction

But until recently we didn't know *how* the cortical brain computes such geometrical entities.

As long as the brain was a "black box", we had no access to the way in which neurons connected together could "do geometry".

6. Introduction

Things changed completely with the introduction of recordings of neural cells (in the late 1950s), and later (in the late 1990s) of revolutionary methods of "in vivo optical imaging" , that made the black box somewhat "transparent".

They enabled to visualize the extremely special connectivity of the primary visual areas, that is their "functional architectures".

These hitherto unknown structures of connectivity enabled to begin to explain the neuronal constitution of perceptual geometry.

Their discovery in the 1990s came as a shock to me, and I recognised in them the neuronal implementation of internal geometric structures that I am going to try to explain.

8. Introduction

What I called "Neurogeometry" is based on the discovery that these *hardwired* and *modular* functional architectures implement structures such as the contact structure and the sub-Riemannian geometry of jet spaces of plane curves.

For principled reasons, it is the *geometrical* reformulation of differential calculus from Pfaff to Lie, Darboux, Frobenius, Cartan and Goursat which turns out to be suitable for neurogeometry.

9. Introduction

As we have to start at the beginning, I will focus on how very local data from a retinal signal can be integrated into global contours.

The key issue I would like to address is the following.

It is an empirical evidence that the visual brain is able to perform a lot of *differential* routines. But how such routines can be *neurally* implemented? At their resolution scale, neurons are “point-like” processors and it seems impossible to compute differential routines with them.

11. Jan Koenderink

The great specialist of vision Jan Koenderink strongly emphasized this crucial point:

> *"[Differential] geometrical features [are] multilocal objects, i.e., in order to compute [boundary or curvature] the processor would have to look at different positions simultaneously [...]. Routines accessing a single location may aptly be called point processors, those accessing multiple locations array processors. The difference is crucial in the sense that point processors need no geometrical expertise at all, whereas array processors do (e.g., they have to know the environment or neighbours of a given location)."*

12. Images of H&W

Let us take a brief look at functional architectures.
The story begins with the breakthrough recordings of V1 neurons in the early 60s by David Hubel and Torsten Wiesel (Nobel prizes in 1981).

These neurons, called "simple", detect a *preferred orientation* p crossing their receptive field centered on a retinal position a. When they are activated they fire and emit spikes and the spikes can be recorded using electrodes.

This is one of the breakthrough images of the history of science.

13. H&W breakthrough

Here are two images of a 40s recording. The little white circles delimit the "receptive field", that is the small domain of the retina to which the neuron responds.
Left: a bar aligned along the preferred orientation (strong firing).
Right: a bar orthogonal to the preferred orientation (quiet, no firing)

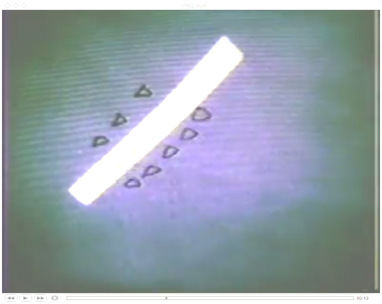

In fact, what Hubel and Wiesel discovered in their pioneering experiment is that the "simple" neurons of $V1$ detect *contact elements* (a, p).

15. Example of receptive profile

To day, we know that it is due to the particular form of of the receptive profiles of these neurons. Level sets of receptive profiles can be recorded. It is an experimental "tour de force".

Here is an example from a cortical neuron in $V1$ (Gregory DeAngelis). The *elongation* of the profile explains the preferred orientation.

16. Example of receptive profile

Left: Level sets of ON (excitatory, red)/OFF (inhibitory, green) zones. Right: model using a third derivative $\varphi(x, y) = \frac{\partial^3 G}{\partial x^3}$).

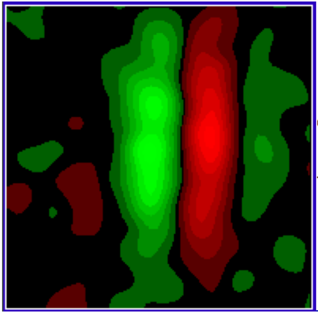

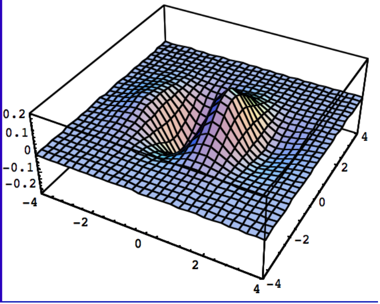

Moreover, Hubel and Wiesel discovered that

Neurons detecting all the orientations p at the same retinal position $a \in \mathbb{R}^2$ constitute an anatomically well delimited small neural module called an "orientation hypercolumn".

and that preferred orientations p vary smoothly with the retinal point a. So the (a, p) constitute an *orientation field*.

18. Braitenberg abduction

The first global reconstruction of an orientation field from the sparse local data provided by electrodes was *infered* abductively in 1979 by Valentino and Carla Braitenberg.

This was long before the introduction of modern *in vivo* optical imaging techniques.

19. Swindale's abduction

After Braitenberg, in an astonishing 1987 paper (still before the advent of optical imaging techniques), Nicholas Swindale reconstructed (for the cat), the "spatial layout" of the orientation map.

He thus confirmed Braitenberg's abduction.

His data came from electrodes separated by about $150 - 300\mu m$ at a cortical depth of about $400 - 700\mu m$.

He succeeded in *interpolating* between the prefered orientations measured at the different sites and reconstructed the "fine grained" map shown in the following figure.

It was a great achievement.

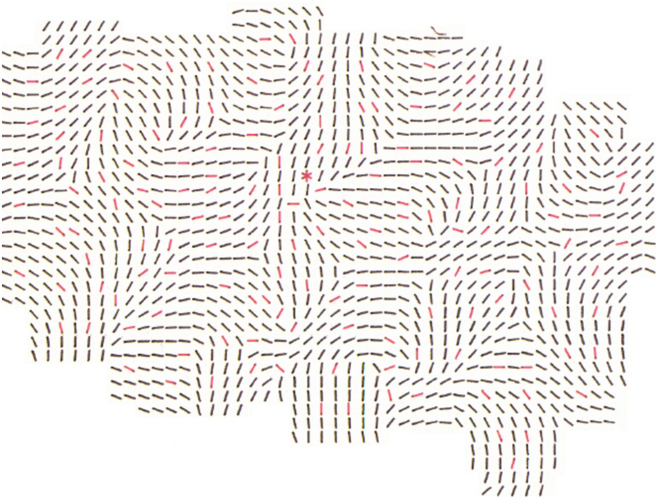

21. Swindale's image 2

Using a color code for directions, he got an orientation map.

This is a theoretical reconstruction from sparse recordings and not an empirical image of the area activity.

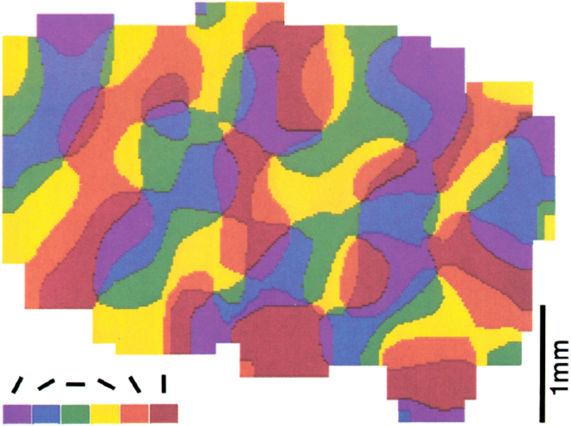

22. In vivo optical imaging

Braitenberg's and Swindale's abductions have been strikingly confirmed in the 1990s by brain imagery and techniques of "in vivo optical imaging based on activity-dependent intrinsic signals" (Amiram Grinvald and Tobias Bonhöffer).

This enables to acquire *in vivo* images of the activity of the superficial cortical layers.

23. In vivo optical imaging II

As Kenichi Ohki and Clay Reid have pointed out,

> *"optical imaging revolutionized the study of functional architecture by showing the overall geometry of functional maps."*

The scale of observation is a "meso"-scale.

For a true "micro"-scale observation at the level of single neurons, you need more recent techniques such as "two-photon confocal microscopy" (Kenichi Ohki 2006).

24. Orientation maps

Here is the functional architecture of the area $V1$ of a tree-shrew (tupaya) obtained by in vivo optical imaging (William Bosking with David Fitzpatrick's team at Duke University).

They used "grattings", that is large grids of parallel dark stripes translated in the visual field.

For every orientation (coded by the bottom-right color) they got a global map of activity (dark = active).

This is now an empirical observation and not a theoretical reconstruction.

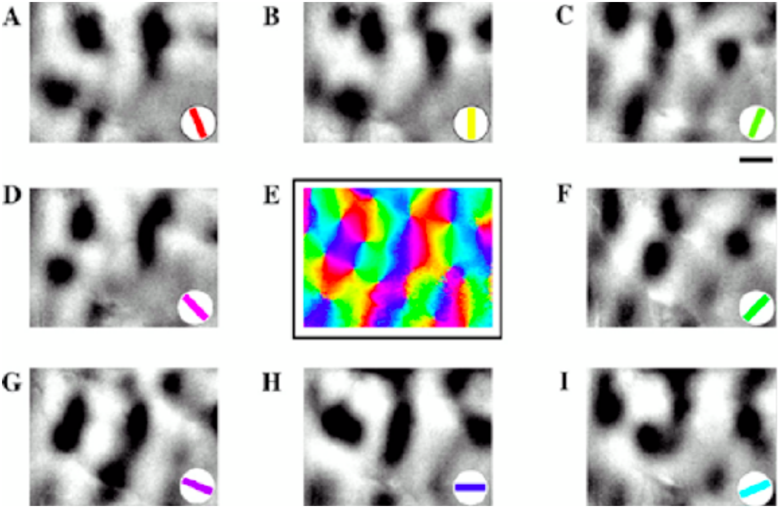
A
B
C
D
E
F
G
H
I

26. Pinwheels

Orientation maps with pinwheels are now well known. Here is the $V1$ area of the macaque by Blasdel and Salama,

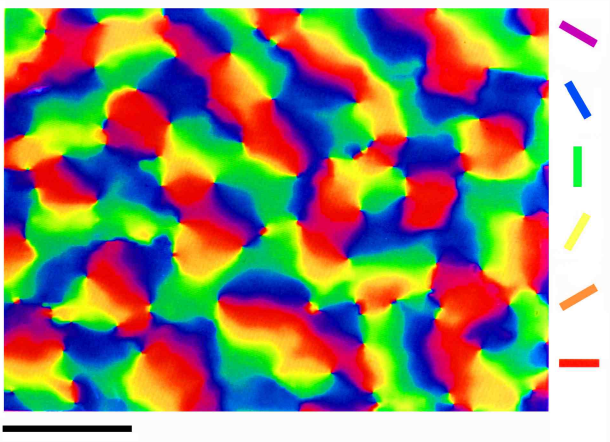

27. End points and triple points

In the following picture due to Shmuel (cat's area 17), orientations are coded by colors but are also represented by small white segments.

We observe very well the two types of generic singularities of 1D foliations in the plane anticipated by Braitenberg and Swindale.

28. Shmuel's orientation map

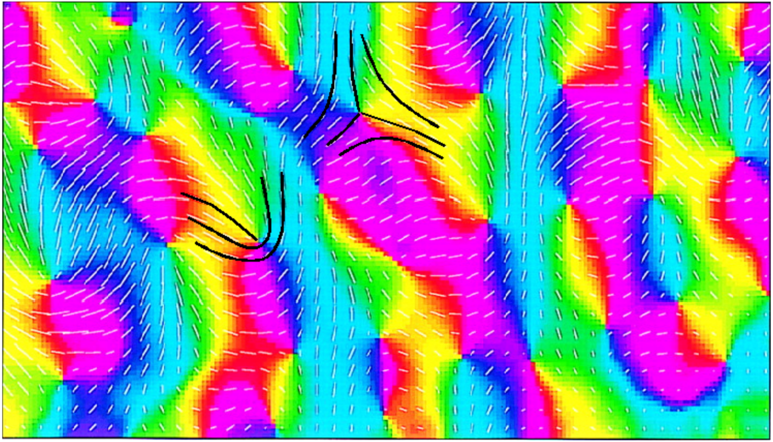

29. Interspecific functional architecture

A pinwheel organisation can be found in many species: cat, primate (marmoset), tupaya (tree shrew), prosimian Bush Baby, tawny owl, etc.

It is a widely interspecific functional architecture.

30. Pinwheels as blowing-up

Pinwheels can be interpreted geometrically as *blowing-up* of points a_i and the orientation field is the closure of a section σ of the fiber bundle $\pi : \mathbb{V}_J = \mathbb{R}^2 \times \mathbb{P}^1 \to \mathbb{R}^2$ (J for "jets") defined over the open subset $\mathbb{R}^2 - \{a_i\}$.

Over the a_i the closure of σ is the "exceptionnal" fiber $\mathbb{P}^1_{a_i}$.

These exceptional fibers $\mathbb{P}^1_{a_i}$ are "contracted" and "folded" onto small wheels around the base points a_i.

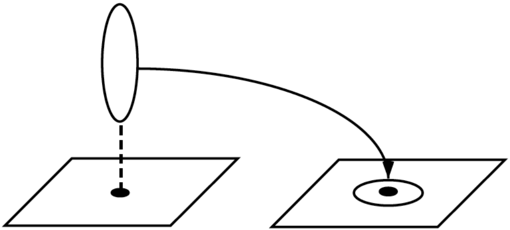

There is therefore a $3D \to 2D$ dimensional collapse : an orientation map is, in a way, a geometric object of "intermediate" dimension between 2 and 3, with a lattice of base points blown-up in parallel,

At the limit, when all the points of the base plane $\mathbb{R}^2$ are blown-up in parallel, we get the fiber bundle $\pi : \mathbb{V}_J = \mathbb{R}^2 \times \mathbb{P}^1 \to \mathbb{R}^2$.

So $\mathbb{V}_J$ can be considered as an *idealized continuous model* of the concrete neural $V1$ produced by biological evolution with its lattice of pinwheels and orientation field.

Let us now come back to the “hard problem”.

The *geometry* of visual perception involves many *differential* computations. But neurons are (scaled) *point-like processors*. When they are actived, they emit spikes defining their “rate coding”. And so, they can only code a single numerical value by means of their “firing rate”.

Of course
(i) they are able to detect point-like cues and
(ii) they are connected and they can transmit their activity along their more or less inhibitory or excitatory connections.

But we must understang why and how this is sufficient to implement differential routines.

33. The antinomy of perceptual geometry.

How differential routines can be neurally implemented in networks of “point-like processors”since derivatives are not point-like entities?

The classical conceptions of “differentiation” and “integration” do not work.

34. Functional connectivity

Now, we have seen that biological evolution has introduced *new post-retinal cortical* modules and layers that implement *new* variables *beyond* the two variables of retinal position.

In particular detectors of contact elements (a, p).

We can therefore try to understand how a connectivity *extended* to these new modules and layers can perform differential computations.

35. The hypothesis

The hypothesis is therefore

Maybe point-like processors can implement an alternative formulation of differential calculus using "hidden derivatives" (Richard Montgomery) as new supplementary *independent* variables which can be implemented in point-like processors.

But these new "hidden" derivatives must satisfy strong *constraints* in order to be interpretable as "true" derivatives (as in Hamiltonian mechanics where you introduce the momenta as new *independent* variables and force them to be dual to velocities using the symplectic 2-form).

For that, *the hardwired connectivity of the network must be extremely specific.*

36. Cortico-cortical horizontal connections

Let us begin with a key experimental discovery.

Orientation hypercolumns correspond to the "vertical" retino-geniculo-cortical connectivity.

But cortical neurons of $V1$ are also connected by "horizontal" cortico-cortical connections *inside the cortical layer itself*.

They are long-ranged (up to 6-8 mm), excitatory, slow (about $0.2\,\text{m}\,/\,\text{s}$) and distributed in a very anisotropic and "patchy" way. It is the key point.

37. A neural parallel transport

It was discovered that such a second system of long-range "horizontal" cortico-cortical connections implements a *parallel transport* enabling the visual system to *compare* two retinotopically neighboring orientation hypercolumns P_a and P_b over two different base points a and b.

38. Horizontal cortico-cortical connections

The following image (due to Bosking *et al.*) shows how a marker (biocytin) locally injected in a zone of about $100\mu m$ of the layer 2/3 of $V1$ of a tupaya (tree shrew) diffuses along horizontal connections (black marks) in a selective, “patchy”, anisotropic way.

Short-ranged diffusion is isotropic and corresponds to *intra*-hypercolumnar inhibitory connections.

On the contrary, long-ranged diffusion is highly anisotropic, and corresponds to excitatory *inter*-hypercolumnar connections

39. Biocytin diffusion

The injection site is upper-left in a blue-green domain.

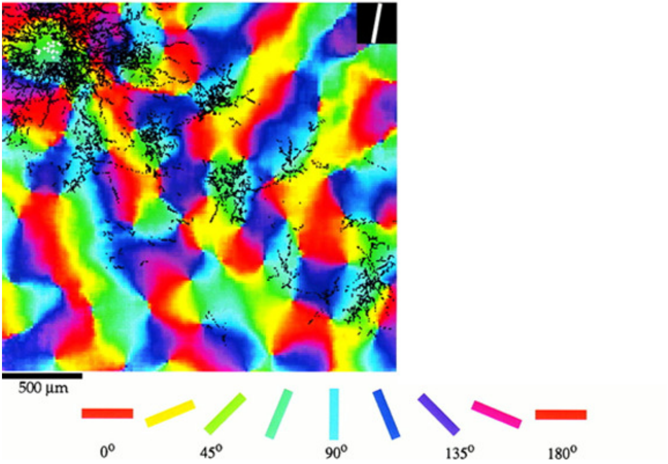

40. Parallelism and co-axiality

There are two main results:

1. The marked axons and synaptic buttons cluster in domains of the *same* blue-green color (same orientation) as the injection site, which means that horizontal connections connect neurons detecting approximately parallel orientation and therefore implement neurally a *parallel transport*.
2. Furthermore, the striking global clustering along the top-left $\longrightarrow$ bottom-right diagonal shows that *almost all* blue-green cells are *without* any marked connections! This crucial empirical fact means that horizontal connections connect neurons detecting not only almost *parallel* but also almost *aligned* "co-axial" orientations.

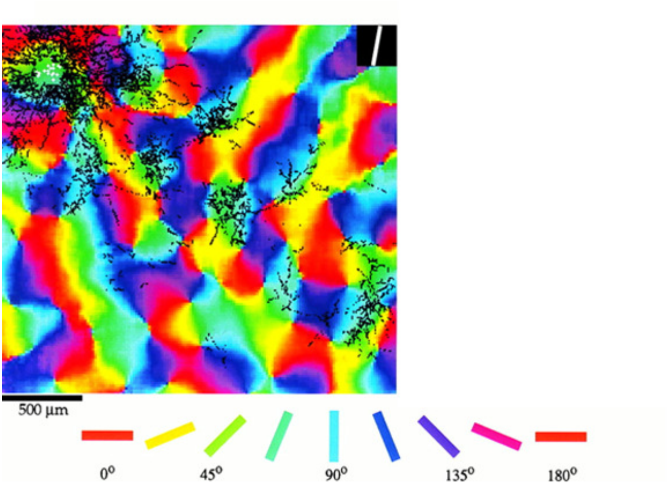
500 µm
0°
45°
90°
135°
180°

So, the key experimental discovery is that

"the system of long-range horizontal connections can be summarized as preferentially linking neurons with co-oriented, co-axially aligned receptive fields."(W. Bosking)

This means neurally that a chain of simple neurons (a_i, p_i) is a chain of *"horizontally" connected* simple neurons iff it is a discretization of the Legendrian lift of a not too curved base curve interpolating between the (a_i).

This means mathematically that,

up to some bound on curvature, the contact structure $\mathcal{C}$ is neurally implemented in $V1$.

Deep experiments of *psychophysics* (Field, Hayes and Hess) concluded also that the *specific connectivity* of $V1$ is characterized by "joint conditions on positions and orientations", which implement one of the fundamental laws of Gestalt theory, that of "good continuation" ("Gesetz der guten Fortsetzung")

44. Cartan comes in

This is where Cartan comes in.

45. Three geometric traditions

In his 1936 lecture at the ICM (Oslo), Cartan commented on the

> *"three main points of view which have dominated the evolution of geometry."*

1. Klein: invariance w.r.t. a given group.
2. Riemann: metric tensor.
3. "Parallelism" and "parallel transport": connections on fiber bundles (his own conception).

The problem is to connect between them the neighboring fibers when one moves in the base M. As noted by Chern and Chevalley in their obituary, it is

> *"to tie up the fibers with the differentiable structure of the base space."*

46. "Point-like processors" can be good differential geometers

But, it is exactly the case of the hypercolumns of $V1$ tied up by horizontal connections as fibers with the retinal base plane. So we can make the hypothesis that it is this very special functional architecture which enables "point-like processors" to be "good differential geometers".

47. The main hypothesis

While the retinal cells detect positions, cortical neurons of $V1$ can detect contact elements and their cortico-cortical connectivity can implement a "geometry of integrability" for these contact elements.

For the cortical low level visual brain integro-differential calculus retinal images is equivalent to a geometry of connectivity between contact elements.

In that sense, the visual brain is a Cartan engine.

So we can say that the cortical visual brain implements the fibration $\mathbb{V} = \mathbb{R}^2 \times \mathbb{P}^1 \longrightarrow \mathbb{R}^2, (a, p) \mapsto a$ with the possibility of interpreting p as an "hidden derivative" (Richard Montgomery), that is as a tangent to a curve.

For that, p must satisfy the fundamental Pfaff equation $\omega = dy - pdx = 0$ defining the contact structure of 1-jets of plane curves.

And functional architecture of cortico-cortical connections implement this Pfaff system.

The distribution $\mathcal{C}$ of contact tangent planes is maximally non integrable since the 3-form

$$\omega \wedge d\omega = (-pdx + dy) \wedge dx \wedge dp = -dx \wedge dy \wedge dp \ .$$

is a volume form, which is the opposite of the Frobenius integrability condition $\omega \wedge d\omega = 0$.

50. Two vocabularies

So, we get a correspondance between two vocabularies, a neurophysiological one and a mathematical one.

simple neurons	(scaled) contact elements (a, p)
R-G-C retinotopy	base space $\mathbb{R}^2$ of positions a
basic / "engrafted" variables	fiber bundle $\mathbb{R}^2 \times P \to \mathbb{R}^2$
orientation hypercolumns and pinwheels	1-jet space $J^1 \subsetneq \mathbb{R}^2 \times P \to \mathbb{R}^2$
◇ long-range horizontal connections, ◇ "co-oriented, co-axially aligned RFs", ◇ "joint constraints on positions and orientations" ◇ "good continuation"	Contact structure

Let us remember that the contact structure $\mathcal{C}$ is left-invariant for a group law making $\mathbb{V}_J$ isomorphic to the (*polarized*) *Heisenberg group* $\mathbb{H}_{pol}$.

$$(x, y, p).(x', y', p') = (x + x', y + y' + px', p + p') \ .$$

Its Lie algebra is generated by the basis of left-invariant fields $X_1 = \frac{\partial}{\partial x} + p\frac{\partial}{\partial y} = (1, p, 0)$ and $X_2 = \frac{\partial}{\partial p} = (0, 0, 1)$ with $[X_1, X_2] = (0, -1, 0) = -\frac{\partial}{\partial y} = -X_3$ (the other brackets $= 0$).

The basis $\{X_1, X_2\}$ of the distribution $\mathcal{C}$ is *bracket generating* (*i.e.* Lie-generates the whole tangent bundle $T\mathbb{V}_J$) (Hörmander condition).

$\mathbb{V}_J = \mathbb{H}_{pol}$ is a *nilpotent* group of step 2 (a Carnot group).

53. The contact structure of $SE(2)$

This can be generalized to the Euclidean group $SE(2)$.

The contact form of $SE(2)$ is

$$\omega_S = \cos(\theta)\, dy - \sin(\theta)\, dx$$

The contact planes are spanned by the tangent vectors $X_1 = \cos(\theta)\frac{\partial}{\partial x} + \sin(\theta)\frac{\partial}{\partial y}$ and $X_2 = \frac{\partial}{\partial \theta}$ with Lie bracket $[X_1, X_2] = \sin(\theta)\frac{\partial}{\partial x} - \cos(\theta)\frac{\partial}{\partial y} = -X_3$ (Reeb vector field).

The distribution $\mathcal{C}$ of contact planes is still bracket generating (Hörmander condition). But $SE(2)$ is no longer nilpotent. It is only solvable.

The Carnot group $\mathbb{V}_J = \mathbb{H}_{pol}$ is its "*tangent cone*", its "nilpotentisation".

I will know focus on long range illusory contours which are one of the most striking phenomenon of low level vision.

Consider for example the well-known Kanizsa triangle. *Local cues* as pacmen and end-points induce very long-range global illusory contours (what is called "modal completion").

56. Curved Kanizsa square

Illusory contours are particularly interesting when they are *curved*.

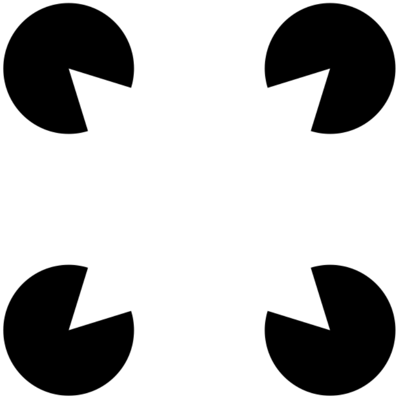

57. Watercolor effect

Furthermore, these contours act as *boundaries for a diffusion of color* inside the square (what is called the "neon" or "watercolor effect").

It is not easily seen on a screen but can be measured with adequate psychophysical methods.

58. Watercolor effect: figure

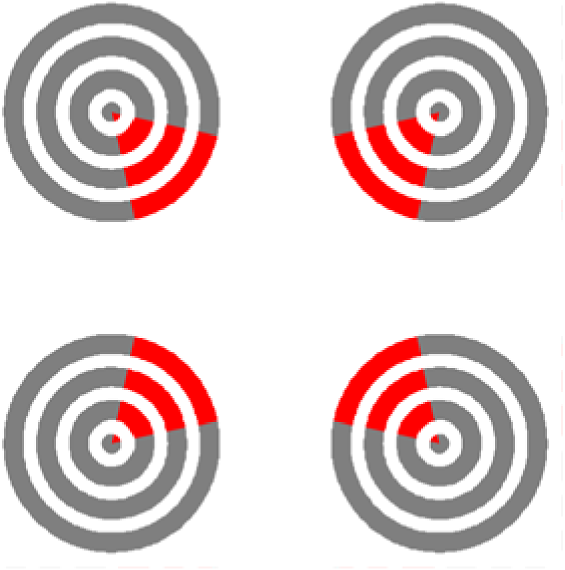

Illusory contours are *neurally real* (Catherine Tallon-Baudry, 1999).

We consider the EEG of an illusory triangle and of a real triangle (three pacmen with global coherence, top of the following figure) and a no-triangle stimulus (three pacmen with no global coherence, bottom of the figure).

60. EEG image

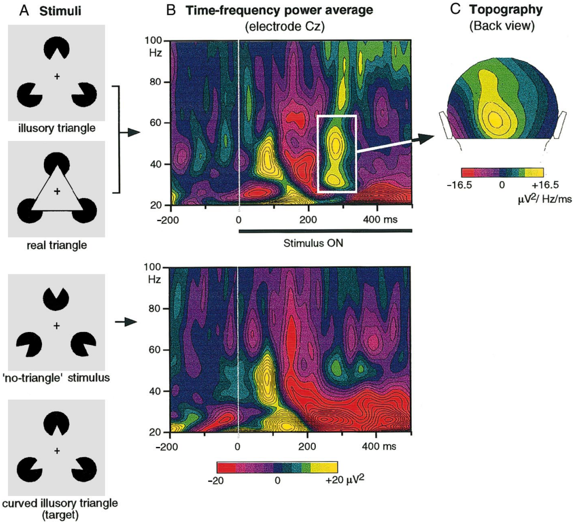

A Stimuli
illusory triangle
real triangle
'no-triangle' stimulus
curved illusory triangle (target)
B Time-frequency power average (electrode Cz)
100 Hz
80
60
40
20
-200
0
200
400 ms
Stimulus ON
-20
0
+20 µV2
C Topography (Back view)
-16.5
0
+16.5
µV2/ Hz/ms

We observe

> *"two successive bursts of oscillatory activities [...]. A first burst at about* 100*ms and* 40*Hz. It showed no difference between stimulus types. A second burst around* 280*ms and* 30-60*Hz. It is most prominent in response to coherent stimuli."*

Yet, the second activation burst, which corresponds to the integration of local sensory data into a global percept, is *the same* for both types of triangles, whether real or illusory, The second burst is framed.

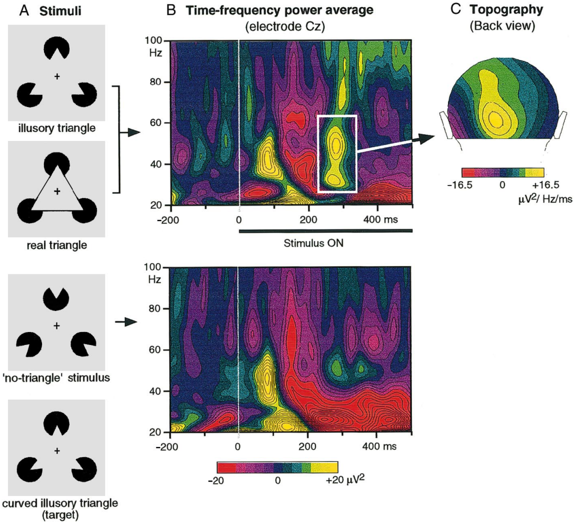

63. Illusory contours as geodesics

I developed the hypothesis that modal illusory contours can be interpreted as *geodesics* of a contact structure for an appropriate metric.

Such sub-Riemannian models have many applications, in particular for *inpainting*, since to complete a corrupted image, we must construct the *illusory level sets* that can complete the missing parts.

Indeed, with sub-Riemannian geodesics and the hypo-elliptic Laplacian, diffusion is possible. It is very anisotropic and leads to very powerful neuromimetic models of inpainting.

Here is a highly corrupted image.

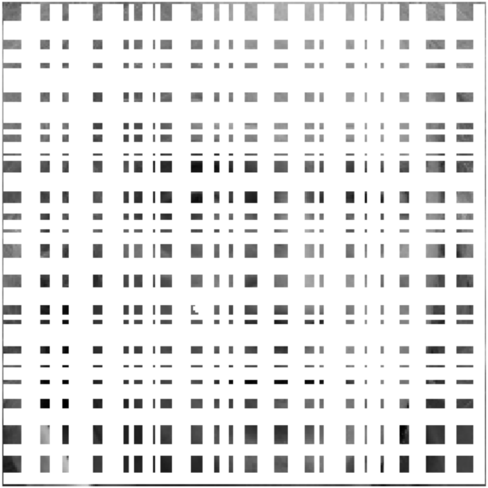

65. An example of sub-Riemannian inpainting

The following picture shows how this highly corrupted image (left) can be very well restored using sub-Riemannian diffusion (Gauthier-Prandi inpainting based on our model).

The face of our friend Jean-Paul Gauthier emerges out of the blue.

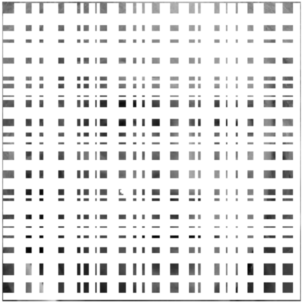

Variational models for illusory contours have been introduced since the late 70s.

1. Shimon Ullman (1976) explained that

   "A network with the local property of trying to keep the contours 'as straight as possible' can produce curves possessing the global property of minimizing total curvature."

2. Berthold Horn introduced in 1983 "the curves of least energy".

These models minimize an energy along curves *in the base plane*.

The best known is the *elastica* model proposed in 1992 by David Mumford.

The energy to minimize is:

$$E = \int_{\gamma} (\alpha\kappa^2 + \beta) ds$$

where γ is a smooth curve in $\mathbb{R}^2$.

68. Geodesic models

But for *neural* models (and not only 2D image processing) it is natural to work in $V1$, that is with the *contact structure* and the *Legendrian lifts*.

It is here that sub-Riemannian geometry fully comes on stage.

The natural idea is to introduce sub-Riemannian metrics on $\mathbb{V}$ and look at geodesic models for curve completion and illusory modal contours.

We take the natural basis $\{X_1, X_2\}$ of the contact plane at the origin as an *orthonormal* basis and we *translate* it using left translations. As the contact structure is left-invariant, we get that way a left-invariant metric on the contact planes.

As this metric is defined only on the contact planes and not on the complete tangent spaces it is sub-Riemannian. But it enables to compute the length of the integral curves of the contact structure, that is of Legendrian lifts.

In the 2000s these problems have been further explored.

(i) Alessandro Sarti and Giovanna Citti began to be interested in Neurogeometry.

(ii) I was fortunate to meet Andrei Agrachev and other very fruitful cooperation on sub-Riemannian geometry quickly started with members of his group, in particular Jean-Paul Gauthier, Ugo Boscain and Yuri Sachkov.

71. The sub-Riemannian $\mathbb{H}_{pol}$

The sub-Riemannian geometry (geodesics, conjugate points, cut locus) of groups such as $\mathbb{H}_{pol}$ or $SE(2)$ is rather complex, even if the groups are elementary.

The sub-Riemannian geometry of the Heisenberg group $\mathbb{H}$ has been explained in the 1980s by Richard Beals, Bernard Gaveau and Peter Greiner.

It can easily be adapted to the polarized $\mathbb{H}_{pol}$.

72. The sub-Riemannian Hamiltonian

The sub-Riemannian sphere S and the wave front W are rather strange. One can compute them explicitly.

Due to the Pontryagin maximum principle, geodesics are the projections on $\mathbb{H}_{pol}$ of the trajectories of a Hamiltonian field defined on the cotangent space.

$$H(x, y, p, \xi, \eta, \pi) = \frac{1}{2}\left[(\xi + p\eta)^2 + \pi^2\right] .$$

where $(x, y, p) = q$ are coordinates in $\mathbb{H}_{pol}$ and (ξ, η, π) coordinates in the cotangent space $T_q\mathbb{H}_{pol}$.

73. Hamilton equations

Hamilton equations on $T\mathbb{V}_J$ are:

$$\begin{cases} \dot{x}(s) = \frac{\partial H}{\partial \xi} = \xi + p\eta \\ \dot{y}(s) = \frac{\partial H}{\partial \eta} = p\left(\xi + p\eta\right) = p\dot{x}(s) \text{ (i.e. } p = \frac{\dot{y}}{\dot{x}} = \frac{dy}{dx}) \\ \dot{p}(s) = \frac{\partial H}{\partial \pi} = \pi \\ \dot{\xi}(s) = -\frac{\partial H}{\partial x} = 0 \\ \dot{\eta}(s) = -\frac{\partial H}{\partial y} = 0 \\ \dot{\pi}(s) = -\frac{\partial H}{\partial p} = -\eta\left(\xi + p\eta\right) = -\eta\dot{x}(s) \ . \end{cases}$$

The moments ξ and η are *constant*, $\xi = \xi_0$ and $\eta = \eta_0$, along any geodesic. Therefore

$$\begin{cases} \dot{x}(s) = \xi_0 + p\eta_0 \\ \dot{y}(s) = p\left(\xi_0 + p\eta_0\right) \\ \dot{\pi}(s) = -\eta_0\left(\xi_0 + p\eta_0\right) \end{cases}$$

Using the variable $\varphi = \frac{\eta_0 \tau}{2}$ associated to the length τ of the geodesic and the constant moment η_0, the sphere $S(0, R)$ and the wave front $W(0, R)$ of $\mathbb{H}_{pol}$ are given by the following equations (where θ is the angle of the tangent).

If (x, p) are expressed in polar coordinates with module $\frac{|\sin(\varphi)|}{\varphi}$, $\varphi > 0$.

$$\begin{cases} x_1 = \frac{|\sin(\varphi)|}{\varphi} \cos(\theta) \\ p_1 = \frac{|\sin(\varphi)|}{\varphi} \sin(\theta) \\ y_1 = \frac{1}{2} x_1 p_1 + \frac{\varphi - \sin(\varphi)\cos(\varphi)}{4\varphi^2} \\ = \frac{1}{2} \frac{\sin^2(\varphi)}{\varphi^2} \cos(\theta) \sin(\theta) + \frac{\varphi - \cos(\varphi)\sin(\varphi)}{4\varphi^2} \\ = \frac{\varphi + 2\sin^2(\varphi)\cos(\theta)\sin(\theta) - \cos(\varphi)\sin(\varphi)}{4\varphi^2} \end{cases}$$

They are displayed in the following figure. The external surface is the sub-Riemannian sphere S. It has a saddle form with singularities at the intersections with the y-axis.

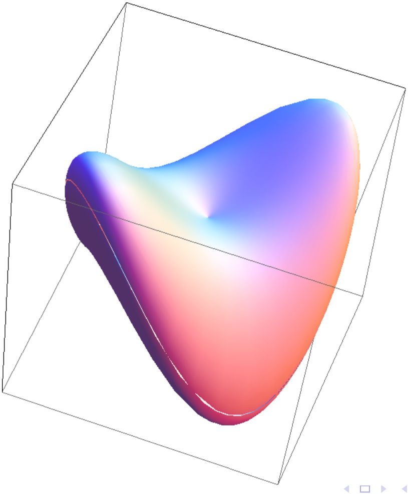

The internal part is $W - S$. It presents smaller and smaller circles of cusp singularities which converge to 0. Such a complex behavior is impossible in Riemannian geometry.

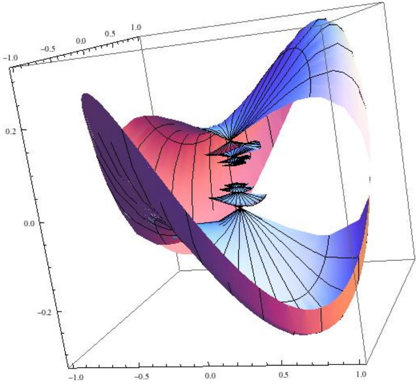

77. The cusps of W

The following figure displays the quarter of the wave front W for $\theta = 0$. Its equations are $x_1 = \frac{|\sin(\varphi)|}{\varphi}$, $p_1 = 0$, $y_1 = \frac{\varphi - \cos(\varphi)\sin(\varphi)}{4\varphi^2}$. The cusps are on the curve of equation $x = \cos(\varphi)$, $y = \frac{1}{4}\cos(\varphi)\sin(\varphi)$.

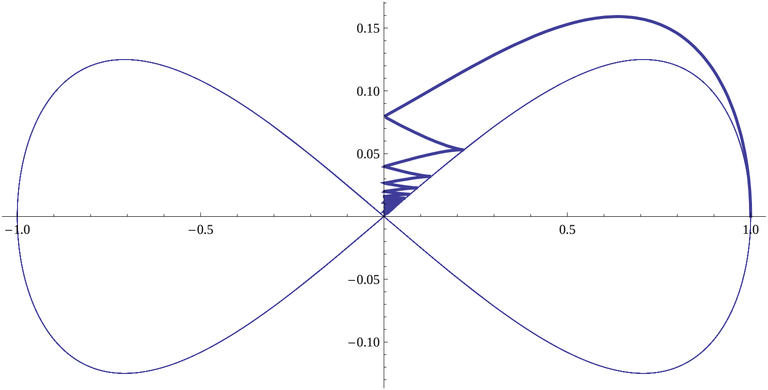

I would now like to present the much more complicated case of $SE(2)$. But I want first note that Pawel Nurowski pointed out to me that we could also use a Cauchy-Riemann structure to do the job.

With the metric g, we can define multiplication by i (intuitively the rotation of ($\frac{\pi}{2}$) in the contact planes K_x, i.e. an isometry J of K_x satisfying the characteristic relation $J^2 = -1$.

1. $d\omega(X, J(Y)) = -d\omega(J(X), Y)$. The 2-form $d\omega$ is called in this context the *Levi form*.
2. $g(J(X), J(Y)) = g(X, Y)$
3. $d\omega(X, Y) = -d\omega(Y, X) = g(X, J(Y))$.

Then we consider the complexification $T\mathbb{V} \otimes_{\mathbb{R}} \mathbb{C}$ of $T\mathbb{V}$, and define the complex fiber bundle $\mathcal{K}_{\mathbb{C}}$ by

$$\mathcal{K}_{\mathbb{C}} = \{X - iJ(X) | X \in \mathcal{K}\}.$$

At each point x, $(\mathcal{K}_{\mathbb{C}})_x$ is complex line.
Indeed if $X - iJ(X)$ is a reference C-vector $\neq 0$ in $(\mathcal{K}_{\mathbb{C}})_x$ and if $Y - iJ(Y)$ is another C-vector in $(\mathcal{K}_{\mathbb{C}})_x$, we have

$$Y - iJ(Y) = (a + ib)(X - iJ(X))$$

with $Y = aX + bJ(X)$ and $J(Y) = -bX + aJ(X)$. In other words, a and b are the components of Y in the basis $\{X, J(X)\}$ of K_x at x.

We have

1. $\mathcal{K}_{\mathbb{C}} \cap \overline{\mathcal{K}}_{\mathbb{C}} = \{0\}$ since $X - iJ(X) = Y + iJ(Y)$ implies both $Y = X$ and $Y = -X$
2. $\mathcal{K}_{\mathbb{C}} \oplus \overline{\mathcal{K}}_{\mathbb{C}} = \mathbb{C}\mathcal{K}$ since, for every $Z \in \mathcal{K}$, $(a + ib)Z$ can be written in a unique way

$$(a + ib)Z = X - iJ(X) + Y + iJ(Y)$$

with $X + Y = aZ$ and $-J(X) + J(Y) = bZ$.

Moreover, while $\mathcal{K}$ is by definition non-integrable since it is a contact structure, $\mathcal{K}_{\mathbb{C}}$ is in contrast integrable in the sense that $[\mathcal{K}_{\mathbb{C}}, \mathcal{K}_{\mathbb{C}}] \subset \mathcal{K}_{\mathbb{C}}$.

Indeed, if we apply the formula

$$d\omega(X, Y) = X(\omega(Y)) - Y(\omega(X)) - \omega([X, Y]) \ ,$$

we see thet, for $X, Y \in \mathcal{K}$, the nullity $\omega(X) \equiv \omega(Y) \equiv 0$ implies

$d\omega(X, Y) = -\omega([X, Y])$ and $d\omega(J(X), J(Y)) = -\omega([J(X), J(Y)])$.

But $d\omega(X, Y) = d\omega(J(X), J(Y))$ and so

$$\omega([X, Y]) = \omega([J(X), J(Y)]),$$

which means that

$$[J(X), J(Y)] - [X, Y] \in \mathcal{K}.$$

In the same way, as $d\omega(X, J(Y)) = -d\omega(J(X), Y)$, we have $-\omega([X, J(Y)]) = \omega([J(X), Y])$, that is

$$[J(X), Y] + [X, J(Y)] \in \mathcal{K}.$$

Let us consider

$$[X - iJ(X), Y - iJ(Y)] \in [\mathcal{K}_{\mathbb{C}}, \mathcal{K}_{\mathbb{C}}], \quad X, Y \in \mathcal{K}.$$

We have

$$[X, J(Y)] + [J(X), Y] = J([X, Y] - [J(X), J(Y)]),$$

which implies

$$\begin{aligned}[X - iJ(X), Y - iJ(Y)] &= [X, Y] - i[X, J(Y)] - i[J(X), Y] - [J(X), \\ &= ([X, Y] - [J(X), J(Y)]) - i([X, J(Y)] + [J \\ &= ([X, Y] - [J(X), J(Y)]) - iJ([X, Y] - [J(X \\ &\in \mathcal{K}_{\mathbb{C}} .\end{aligned}$$

This structure defines a *Cauchy-Riemann* manifold.

With Giovanna Citti and Alessandro Sarti we studied the passage from the $\mathbb{V}_J$ bundle, with its natural action of the Euclidean group $\mathbb{R}^2 \rtimes \mathbb{S}^1 = SE(2)$, to $SE(2)$ itself.

We thus go to the model $SE(2) = \mathbb{V}_S$ endowed with its natural contact structure and its associated L-invariant sub-Riemannian metric.

The geometry of the sub-Riemannian spheres and wavefronts is much more complicated. It was computed in the 2000s by Andrei Agrachev, Yuri Sachkov, Igor Moiseev, Ugo Boscain, Jean-Paul Gauthier.

We have seen that the contact 1-form is $\omega_S = \omega = -\sin(\theta)\,dx + \cos(\theta)\,dy$ and the basis of contact planes is $X_1 = \cos(\theta)\,\partial_x + \sin(\theta)\,\partial_y$ and $X_2 = \partial_\theta$ with Lie bracket $[X_1, X_2] = \sin(\theta)\,\partial_x - \cos(\theta)\,\partial_y = X_3$, and $-X_3$ being the Reeb field.

The Legendrian lifts of curves (i.e. the integral curves of the contact structure $\mathcal{K}$) are solutions of the controled differential system:

$$\begin{cases} \dot{x} = u_1 \cos(\theta) \\ \dot{y} = u_1 \sin(\theta) \\ \dot{\theta} = u_2 \end{cases} \tag{1}$$

We want to minimize the length of Legendrian curves. For that we use the Pontryagin Maximum Principle.

We work in the cotangent space $T^*\mathbb{V}_S$ of $\mathbb{V}_S = SE(2)$. The minimization is expressed by an Hamiltonian H giving trajectories in $T^*\mathbb{V}_S$ whose projections on $\mathbb{V}_S$ are the geodesics.

We start with the kinetic energy defined on the tangent fiber bundle $T\mathbb{V}_S$

$$\dot{q}^2 = (u_1 \cos(\theta))^2 + (u_1 \sin(\theta))^2 + u_2^2 = u_1^2 + u_2^2$$

We take the Legendre transform defined on the cotangent fiber bundle $T^*\mathbb{V}_S$)

$$h(\lambda, q) = \langle \lambda, \dot{q} \rangle - \frac{1}{2}\dot{q}^2$$

λ being a covector $\lambda = (\lambda_x, \lambda_y, \lambda_\theta)$ in the base $dx, dy, d\theta$ of $T^*\mathbb{V}_S$.

According to the PMP, we get the Hamiltonian of geodesics by maximizing $h(\lambda, q)$ w.r.t. the controls u_1 et u_2.

88. The Hamiltonian of $SE(2)$

If λ_1, λ_2, λ_3 are the components of the covector λ in the basis $(\omega_1, \omega_2, \omega_3)$ dual to (X_1, X_2, X_3) (i.e. $\lambda_i = \langle \lambda, X_i \rangle$), the Hamiltonian giving the geodesics is

$$H(\lambda, q) = \frac{1}{2}\left(\lambda_1^2 + \lambda_2^2\right)$$

That is

$$H(\lambda, q) = \frac{1}{2}\left((\lambda_x \cos(\theta) + \lambda_y \sin(\theta))^2 + \lambda_\theta^2\right)$$

with

$$\{\lambda_1 = \lambda_x \cos(\theta) + \lambda_y \sin(\theta), \lambda_2 = \lambda_\theta, \lambda_3 = \lambda_x \sin(\theta) - \lambda_y \cos(\theta)\}$$

Now, a key point is that there exists a *pendulum equation* behind this Hamiltonian formulation of geodesics. I remember when Andrei Agrachev explained me that point.

H is constant along trajectories. If $H = \frac{1}{2}$, $\lambda_1^2 + \lambda_2^2 = 1$ and if we take $\lambda_1 = \sin\left(\frac{\gamma}{2}\right)$, $\lambda_2 = -\cos\left(\frac{\gamma}{2}\right)$, then γ satisfies the *pendulum equation*

$$\ddot{\gamma} = -\sin(\gamma)$$

and Hamilton equations become

$$\begin{cases} \dot{x} = \sin\left(\frac{\gamma}{2}\right)\cos(\theta) = \lambda_1 \cos(\theta) \\ \dot{y} = \sin\left(\frac{\gamma}{2}\right)\sin(\theta) = \lambda_1 \sin(\theta) \\ \dot{\theta} = -\cos\left(\frac{\gamma}{2}\right) = \lambda_2 \\ \ddot{\theta} = \frac{1}{2}\sin\left(\frac{\gamma}{2}\right)\dot{\gamma} = \dot{\lambda}_2 \end{cases}$$

And so, a motion $\gamma(t)$ of the pendulum generates a geodesic.

We put $\dot{\gamma} = c$.
The energy of the pendulum is
$E = \frac{1}{2}(\dot{\gamma})^2 - \cos(\gamma) = \frac{1}{2}(c)^2 - \cos(\gamma)$. Its minimum is -1.

The phase portrait $\mathcal{C}$ of the pendulum in the $(\gamma, \dot{\gamma} = c)$ plane is given by the level lines of E. It is stratified and decomposes into strata of respective dimensions 2, 1, 0 (i.e. of codimension 0, 1, 2).

Its stratification drives the classification of geodesics (as we use $\frac{\gamma}{2}$, we consider that γ has period 4π).

92. The pendulum phase portrait

In magenta: open stratum C_1 (2 connected components, oscillations). In yellow: open stratum C_2 (2 connected components, rotation). In thick lines: the 1-dimensional stratum C_3 (4 connected components). Point strata C_4 (2 points, stable equilibrium) and C_5 (2 points, unstable equilibrium).

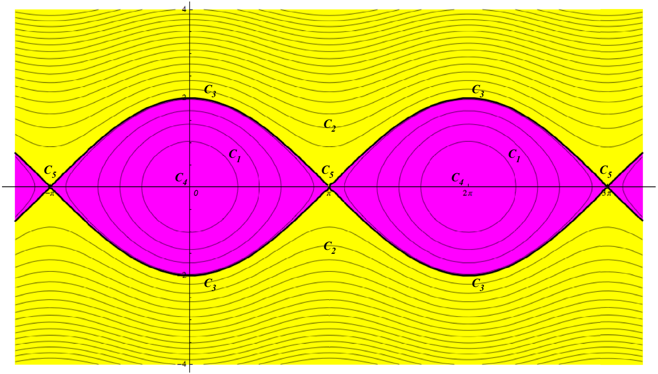

93. The pendulum phase portrait

The periods T of the pendulum are given by the complete elliptic integral of the first kind

$$K(k) = \int_0^{\frac{\pi}{2}} \frac{dt}{\sqrt{1 - k^2 \sin^2 t}}$$

where k is the module.

- if $(\gamma, c) \in C_1$ (oscillating pendulum), then $c \in (0, 2)$, $E \in (-1, 1)$,

$$k_1 = \sqrt{\frac{E+1}{2}} = \sqrt{\frac{c^2}{4} + \sin^2\left(\frac{\gamma}{2}\right)} \in (0, 1)$$

  ($k_1 = \frac{c}{2}$ for $\gamma = 0$) and $T = 4K(k_1)$.

- If $(\gamma, c) \in C_2^+$ (rotating pendulum), then $c \in (2, \infty)$, $E > 1$,

$$k_2 = \sqrt{\frac{2}{E+1}} = \frac{1}{\sqrt{\frac{c^2}{4} + \sin^2\left(\frac{\gamma}{2}\right)}} \in (0, 1)$$

  ($k_2 = \frac{2}{c}$ for $\gamma = 0$) and $T = 2K(k_2)\, k_2$.

  The k_2 factor is essential and explains why the C_2 part generates a sub-Riemannian geometry much more complicated than the C_1 part.

- At the limit $E = 1$, we have $T = \infty$.

The point $(\gamma_0 = 0, c_0)$ individuates the pendulum trajectory. The map sending $(c_0, t) \in \mathbb{R}^+_{(c)} \times \mathbb{R}_{(t)}$ to the point (γ_t, c_t) of the trajectory is analytic.
If we quotient it by the periods we get a *diffeomorphism* Φ and we can consider the inverse $F = \Phi^{-1}$.

$$F(\gamma, c) = (c_0, \varphi)$$

that is $(\gamma, c) = (\gamma_\varphi, c_\varphi)$.

$\varphi(\gamma, c)$ is the retrograde time the pendulum would take to return from (γ, c) to $(\gamma_0 = 0, c_0)$.

Yuri Sachkov then computed the sub-Riemannian geometry of $\mathbb{V}_S = SE(2)$ using *Jacobi coordinates* (φ, k) which "rectify" the dynamics of the pendulum $\ddot{\gamma} = -\sin(\gamma)$.

> *"Elliptic coordinates lift the veil of complexity over the problems governed by the pendulum equation and open their solution to our eyes."*

In these coordinates, the "vertical" system in the fibers becomes trivial because $\dot{k} = 0$ and $\dot{\varphi} = 1$, i.e. $\varphi_t = \varphi + t$ with $\varphi = \varphi_0$. k is the modulus of the elliptic integral associated with the pendulum: it encodes the energy E; φ_t is the "pendular" time-length: it encodes the length of the geodesic.

97. Jacobi functions

Remember that, given the integral

$$\Phi(\Theta) = \int_0^{\Theta} \frac{d\psi}{\sqrt{1 - k^2 \sin^2(\psi)}} ,$$

the angle $\Theta(\Phi)$ which is the inverse fonction of $\Phi(\Theta)$ is the "amplitude" $\mathrm{am}(\Phi)$ of $\Phi(\Theta)$.

The Jacobi functions are

$$\mathrm{cn}(\Phi) = \cos(\Theta) \text{ and } \mathrm{sn}(\Phi) = \sin(\Theta)$$

$$\mathrm{cn}^2(\Phi) + \mathrm{sn}^2(\Phi) = 1 .$$

$$\mathrm{dn}(\Phi) = \sqrt{1 - k^2 \mathrm{sn}^2(\Phi)} .$$

For the C_1^0 stratum, Sachkov and Moiseev found (with $x_t = x(t)$, etc., and $\mathbb{E}(\varphi) = \int_0^\varphi \mathrm{dn}^2(r,k)\,dr$),

$$\begin{cases} c = 2k\,\mathrm{cn}(\varphi,k) \\ \sin\left(\frac{\gamma}{2}\right) = k\,\mathrm{sn}(\varphi,k) \text{ and } \cos\left(\frac{\gamma}{2}\right) = \mathrm{dn}(\varphi,k) \\ \cos(\theta_t) = \mathrm{cn}(\varphi,k)\,\mathrm{cn}(\varphi_t,k) + \mathrm{sn}(\varphi,k)\,\mathrm{sn}(\varphi_t,k) \\ \sin(\theta_t) = \mathrm{sn}(\varphi,k)\,\mathrm{cn}(\varphi_t,k) - \mathrm{cn}(\varphi,k)\,\mathrm{sn}(\varphi_t,k) \\ x_t = \frac{1}{k}\left(\mathrm{cn}(\varphi,k)\left(\mathrm{dn}(\varphi,k) - \mathrm{dn}(\varphi_t,k)\right) + \mathrm{sn}(\varphi,k)\left(t + \mathbb{E}(\varphi) - \mathbb{E}(\varphi_t)\right)\right) \\ y_t = \frac{1}{k}\left(\mathrm{sn}(\varphi,k)\left(\mathrm{dn}(\varphi,k) - \mathrm{dn}(\varphi_t,k)\right) - \mathrm{cn}(\varphi,k)\left(t + \mathbb{E}(\varphi) - \mathbb{E}(\varphi_t)\right)\right) \\ \theta_t = sg_1\left(\mathrm{am}(\varphi) - \mathrm{am}(\varphi_t)\right) \mod (2\pi) \; (sg_1 = \text{ sign of} \cos\left(\frac{\gamma}{2}\right)) \; . \end{cases}$$

where the last formula for θ_t follows from the formulas

$$\cos(\mathrm{am}(\varphi)) = \mathrm{cn}(\varphi,k)\,, \quad \sin(\mathrm{am}(\varphi)) = \mathrm{sn}(\varphi,k)$$

They are composed with Jacobi elliptic functions of φ and $\varphi_t = \varphi + t$.

For the C_2 stratum, Sachkov and Moiseev found

$$\begin{cases} c = sg_2 \frac{2}{k} \mathrm{dn}\left(\frac{\varphi}{k}, k\right) \;\; (sg_2 = \text{sign of } c) \\ \sin\left(\frac{\gamma}{2}\right) = sg_2 \mathrm{sn}\left(\frac{\varphi}{k}, k\right) \\ \cos\left(\frac{\gamma}{2}\right) = \mathrm{cn}\left(\frac{\varphi}{k}, k\right) \\ \cos(\theta_t) = k^2 \mathrm{sn}\left(\frac{\varphi}{k}, k\right) \mathrm{sn}\left(\left(\frac{\varphi}{k}\right)_t, k\right) + \mathrm{dn}\left(\frac{\varphi}{k}, k\right) \mathrm{dn}\left(\left(\frac{\varphi}{k}\right)_t, k\right) \\ \sin(\theta_t) = k\left(\mathrm{sn}\left(\frac{\varphi}{k}, k\right) \mathrm{dn}\left(\left(\frac{\varphi}{k}\right)_t, k\right) - \mathrm{dn}\left(\frac{\varphi}{k}, k\right) \mathrm{sn}\left(\left(\frac{\varphi}{k}\right)_t, k\right)\right) \\ x_t = sg_2 k \begin{pmatrix} \mathrm{dn}\left(\frac{\varphi}{k}, k\right)\left(\mathrm{cn}\left(\frac{\varphi}{k}, k\right) - \mathrm{cn}\left(\left(\frac{\varphi}{k}\right)_t, k\right)\right) \\ +\mathrm{sn}\left(\frac{\varphi}{k}, k\right)\left(\frac{t}{k} + \mathbb{E}\left(\frac{\varphi}{k}\right) - \mathbb{E}\left(\left(\frac{\varphi}{k}\right)_t\right)\right) \end{pmatrix} \\ y_t = sg_2 \begin{pmatrix} k^2 \mathrm{sn}\left(\frac{\varphi}{k}, k\right)\left(\mathrm{cn}\left(\frac{\varphi}{k}, k\right) - \mathrm{cn}\left(\left(\frac{\varphi}{k}\right)_t, k\right)\right) \\ -\mathrm{dn}\left(\frac{\varphi}{k}, k\right)\left(\frac{t}{k} + \mathbb{E}\left(\frac{\varphi}{k}\right) - \mathbb{E}\left(\left(\frac{\varphi}{k}\right)_t\right)\right) \end{pmatrix} \end{cases}$$

100.Geodesics, spheres and wavefronts

So geodesics are functions of three variables (φ, k, t)
$\{x(\varphi, k, t) = x_t(\varphi, k), y(\varphi, k, t) = y_t(\varphi, k), \theta(\varphi, k, t) = \theta_t(\varphi, k)\}$

t is the time and the length.

When (φ, k) is given and t is variable we follow a geodesic.

When t is given and (φ, k) vary we get surfaces which are the sub-Riemannian spheres $S(0, R)$ and wave fronts $W(0, R)$.

101. The SR spheres $S(0,R)$ and wavefronts $W(0,R)$ of $SE(2)$

The sub-Riemannian spheres $S(0,R)$ and wavefronts $W(0,R)$, $S(0,R) \subset W(0,R)$, of $\mathbb{V}_S = SE(2)$ look a bit like those of the polarized Heisenberg group (the tangent nilpotentisation of $SE(2)$), but are much more complicated.

A fundamental difference is that the y-axis, which was a degenerate caustic in the $\mathbb{V}_J$ case, splits into four cusp branches of an astroidal cone and the point singularities on the y-axis in the $\mathbb{V}_J$ case unfold into small "tetrapaks".

We illustrate first the case $R = \frac{\pi}{2}$. The strata C_i are sent by the exponential map into strata $W_{C_i,\frac{\pi}{2}}$ of $W\left(0,\frac{\pi}{2}\right)$. The following figure displays two viewpoints on $W_{C_1,\frac{\pi}{2}}$ as well as $W_{C_3,\frac{\pi}{2}}$.

102. $W_{C_{1\&3},\frac{\pi}{2}}$

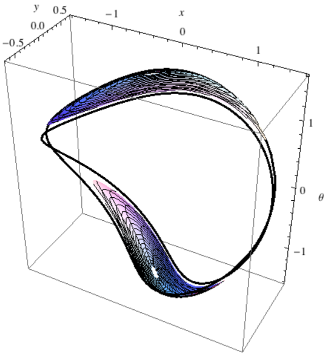

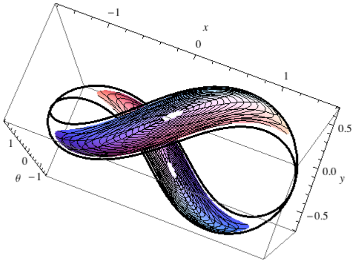

The images of the $C_2^{\pm}$ strata are much more complicated, with an infinity of singularities accumulating on the origin.

Let us consider the image $W_{C_2^+, \frac{\pi}{2}}$ of C_2^+ with its level lines L_k for $k = \text{cst}$. The figure shows some of them from two viewpoints. They are twisted circles with highly oscillating mean "radius" converging to 0.

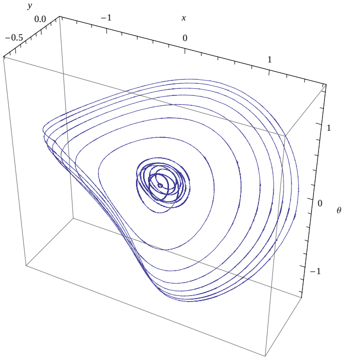
y
0.0
−0.5
−1
x
0
1
1
0
θ
−1

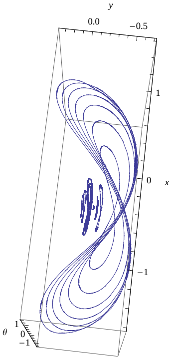
y
0.0
−0.5
1
0
x
−1
θ
1
0
−1

$W_{C_2^+, \frac{\pi}{2}}$ for $k \in (0.07, 0.8)$.

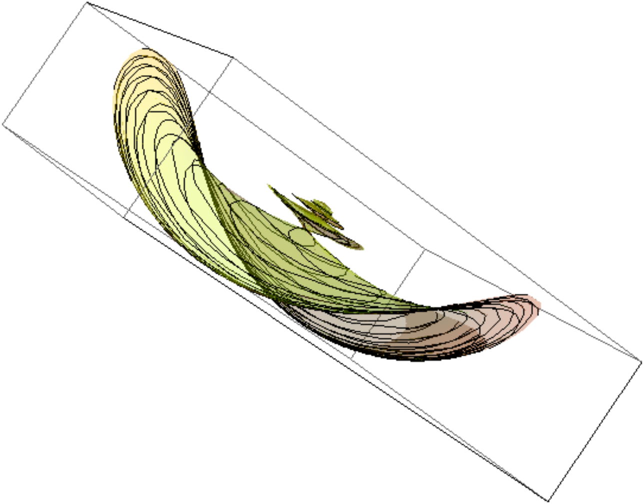

In the formulas for strata C_1 and C_2, the Jacobi elliptic functions have a period $T_1(k) = 4K(k)$ for C_1 and $T_2(k) = 4kK(k)$ for C_2, where $K(k)$ is the complete elliptic integral of the first kind.

As $\varphi_t = \varphi + t$, then, if k is such that $t = R = nT(k)$, the formulas can be simplified.

Let us take $n = 1$.

For C_1, as $K(k) \geqslant \frac{1}{2}\pi$, there exists a solution k_R only if $t = R \geq 2\pi$.

But for C_2 (e.g. C_2^+) there exists *always* a solution k_R of $t = R = 4kK(k)$ and then, for $k = k_R$, we get exceptional level lines.

And as $\operatorname{sn}(\varphi + 2K, k) = -\operatorname{sn}(\varphi, k)$ while $\operatorname{dn}(\varphi + 2K, k) = \operatorname{dn}(\varphi, k)$, the exceptional level line L_{k_R} is *degenerate* since y_R being of period only $2K$ takes twice the same value.

I made some pictures.

We have $k_{\frac{\pi}{2}} \sim 0.246139$. For $k_{c,\frac{\pi}{2}} \sim 0.2541$ neighbor of $k_{\frac{\pi}{2}} \sim 0.246139$ and solution of a more complex equation found by Sachkov, there exists another degenerate level line $L_{k_{c,\frac{\pi}{2}}}$ ("c" for critical). The geometry of the wave-front $W\left(0, \frac{\pi}{2}\right)$ between these values is particular.

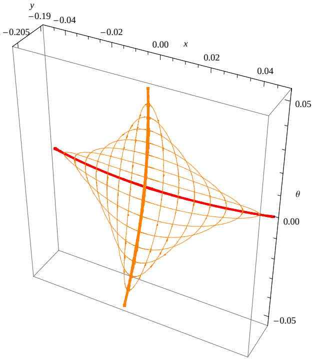

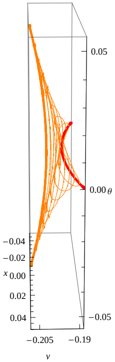

This geometry of transition between L_{k_R} and $L_{k_{c,R}}$ unfolds the singular points on the y-axis in the Heisenberg case.

It has the shape of a “tetrapak” of which a simple model is represented in the following figure

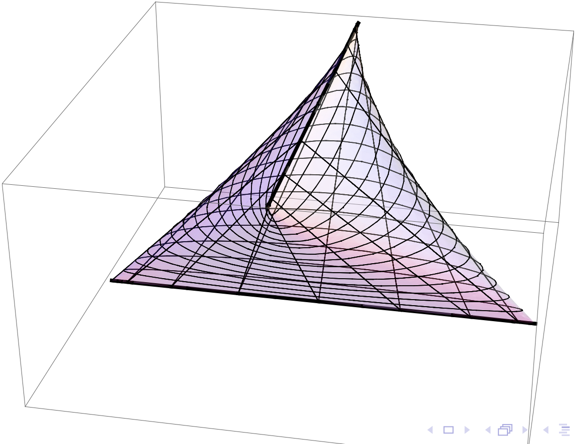

The following figure shows the front $W\left(0, \frac{\pi}{2}\right)$ for $k \in [0.24, 0.26]$ with the "tetrapak" transition between the degenerate level lines $k_{\frac{\pi}{2}} \sim 0.246139$ and $k_{c,\frac{\pi}{2}} \sim 0.254126$.

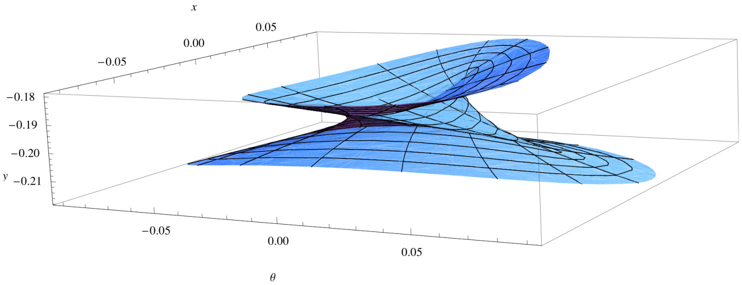

When the radius R varies, the ends of the degenerate level lines L_{k_R} and $L_{k_{c,R}}$ run along four branches which split the y-axis of the Heisenberg case (caustic).

The figure displays the L_{k_R} (in red) and the $L_{k_{c,R}}$ (in orange) for R varying from 0 to $\frac{3\pi}{2}$ in steps of $\frac{\pi}{6}$.

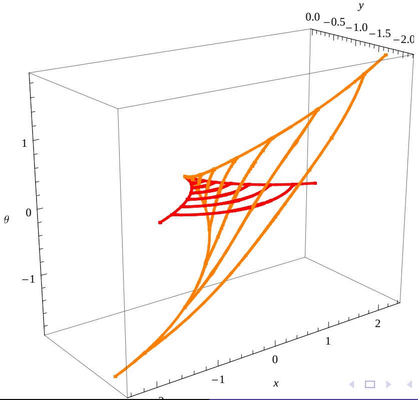

Next figure displays (with two viewpoints) the sphere $S\left(0, \frac{\pi}{2}\right)$ and the wavefront $W\left(0, \frac{\pi}{2}\right)$ for $k \leq 0.8$.

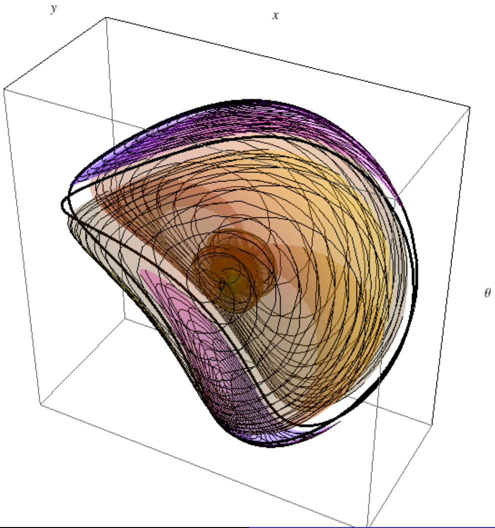

114. $SE(2)$ wave front

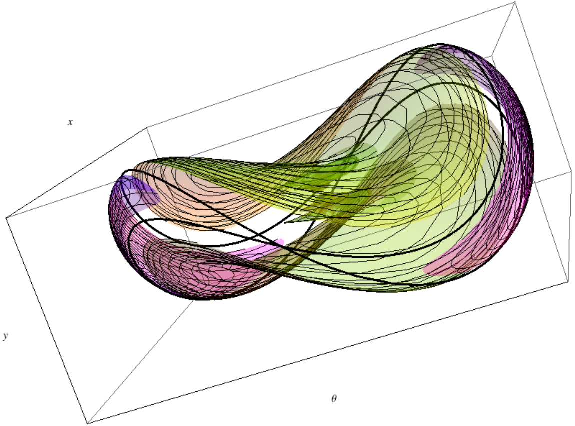

As the radius R of the sphere $S(0,R)$ and of the wavefront $W(0,R)$ increases, the distortions increase.

Next figure shows four viewpoints on the image $W_{C_1^0, R=\frac{3\pi}{2}} \cup W_{C_1^{2\pi}, R=\frac{3\pi}{2}}$ of the strata C_1^0 and $C_1^{2\pi}$ at time-length $t = R = \frac{3\pi}{2}$ for $k \in [0.1, 0.999]$ as well as the image $W_{C_3, R=\frac{3\pi}{2}}$ of the four C_3 strata which bound them.

Remark: the angle θ is not represented modulo 2π.

116. $W_{C_1^0, R=\frac{3\pi}{2}} \cup W_{C_1^{2\pi}, R=\frac{3\pi}{2}}$

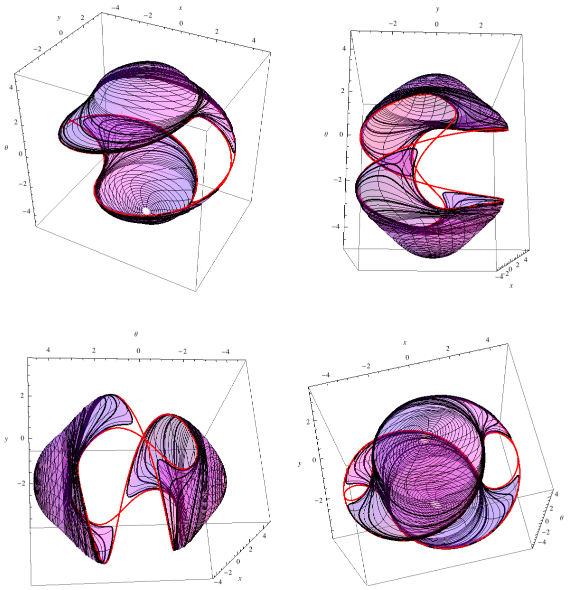

117. $W_{C_2^+, R=\frac{3\pi}{2}}$

Even more than in the case $R = \frac{\pi}{2}$, the images $W_{C_2^+, R=\frac{3\pi}{2}}$ of the strata $C_2^{\pm}$ are much more complicated with their infinity of singularities. The next figure shows some level lines L_k for $k = \text{cst}$ as well as the way in which the half profile P_0^+ of $W_{C_2^+, R=\frac{3\pi}{2}}$ (in red) intersects these level lines of level L_k when spiraling towards 0.

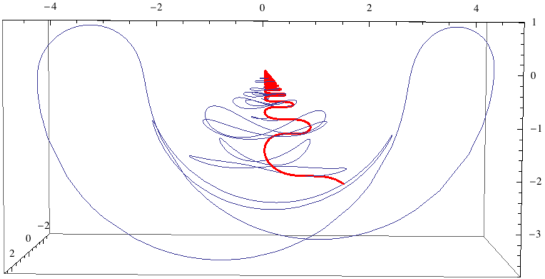

Next figure represents the image $W_{C_2^+, R=\frac{3\pi}{2}}$ of C_2^+ for $k \in [0.01, 0.999]$.

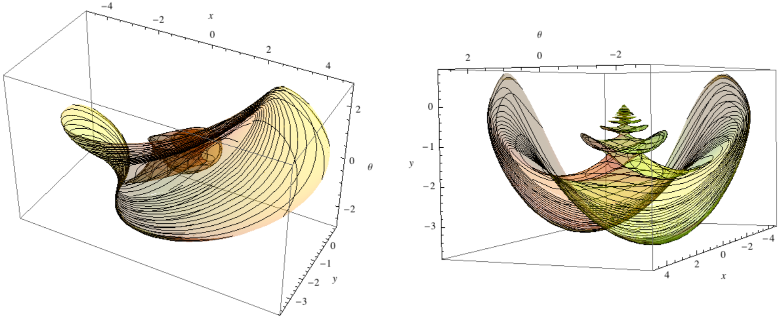

Next figure shows how $W_{C_2^+, R=\frac{3\pi}{2}}$ fits into $W_{C_1^0, R=\frac{3\pi}{2}} \cup W_{C_1^{2\pi}, R=\frac{3\pi}{2}}$.

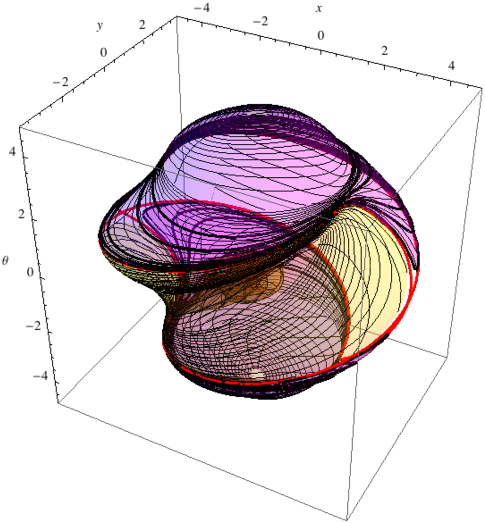

Next figures show two perspectives on the complete wavefront $W\left(0,\frac{3\pi}{2}\right)=W_{C_1^0,R=\frac{3\pi}{2}}\cup W_{C_1^{2\pi},R=\frac{3\pi}{2}}\cup W_{C_2^+,R=\frac{3\pi}{2}}\cup W_{C_2^-,R=\frac{3\pi}{2}}$.

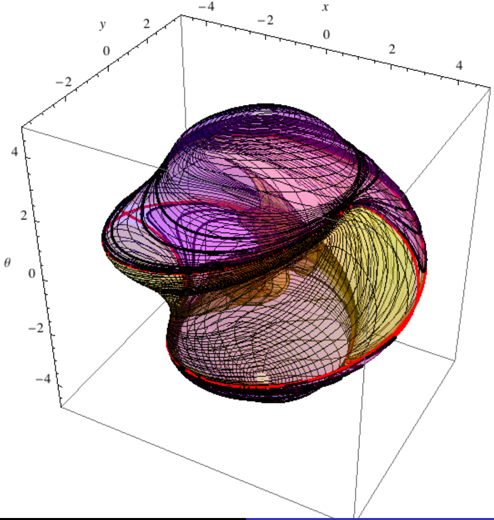

121. Complete wavefront II